Numerical Simulation of Laminar and Turbulent Two-Phase Flow in Pressure-Swirl Atomizers

A. Nouri-Borujerdi[1] and A. Kebriaee[2]

School of Mechanical Engineering, Sharif University of Technology, Tehran, Iran, P. O. Box 11155-9567

This paper has developed an axisymmetric laminar and turbulent two-phase flow solver to simulate pressure swirl atomizer. Equations include explicit algebraic Reynolds stress model, Reynolds averaged Navier Stokes and level set equation. Applying high order compact upwind finite difference scheme with the level set equation being culminated to capture the interface between air-liquid two-phase flow and decreasing the mass conservation error in the level set equation. The results show that close to swirl chamber wall and to axis, some recirculation zones are observed. Converting Rankin vortex from the swirl chamber to forced vortex in orifice section can be predicted by this model. The proposal model shows a considerable improvement in the numerical results especially in laminar flow so that the discharge coefficient, film thickness, and spray cone angle are satisfactory with the previous experimental data. In addition, the error is less than 10 percent.

Key words: pressure swirl atomizer, turbulent flow, explicit algebraic Reynolds stress model, level set

Nomenclature

A	=	area (mm^2)
C_D	=	discharge coefficient
D	=	Differential operator
d	=	diameter (mm)
g	=	gravity acceleration (m/s^2)
H	=	Heaviside function
I	=	turbulent intensity

[1] Professor, School of mechanical Engineering, anouri@sharif.edu
[2] Ph. D. candidate, School of mechanical Engineering, kebriaee@mech.sharif.edu

k = turbulent kinetic energy (m^2/s^2)

L = length (mm)

p = pressure (N/m^2=pa)

Q = volume flow rate (m^3/s)

r = r-coordinate (m)

S = source term, smoothed function

t = time (t)

u = velocity (m/s)

x = space vector

z = z-coordinate (m)

Greek

α = spray cone angle

ε = turbulent dissipation rate (m^2/s^3)

ϕ = level set function (m)

η = η-direction, curvilinear coordinate

λ = free parameter in level set equation

μ = viscosity coefficient

θ = θ-direction

ρ = density (kg/m^3)

τ = virtual time (t)

ξ = ξ-direction, curvilinear coordinate

Subscripts

g = gas

l = liquid

i = inlet port

o = outlet

s = swirl chamber

I. Introduction

Pressure-swirl atomizer is widely used in many industrial applications such as fuel injection in gas turbine, internal combustion engine and liquid-fuel rocket, spray drying, spray in firing and agricultural nozzles. Despite of simple geometry and operation of a pressure-swirl atomizer, flow behavior through it is complicated due to the strongly swirling velocity component and induced air core in the axial zone. During operation of an injector, liquid is fed into swirl chamber via two or more tangential inlet slots. After crossed through device, a strongly swirling flow is imported to the outlet part called orifice and is finally emitted from it. Highly increased tangential velocity leads to create a low pressure zone in the center of the injector. Subsequently, air is pulled into the low pressure region and the induced air core is formed. Due to the air core, an emanated hollow cone shaped liquid is formed with a strongly unstable property from the thin liquid layer with high swirling velocity. The most contribution study on the pressure-swirl atomizer devotes to the experimental observations to detect injector geometric characteristics and functional parameters relation, [1]. Few numerical and experimental works have been conducted to recognize internal flow behavior. Yule and Chinn et al. [2-4] are pioneer in simulation of two-phase flow in the simplex atomizers. They predicted numerically the air core shape in the pressure-swirl atomizer. They observed Gortler wall vortices and central recirculation zones in CFD simulations confirmed with the experimental measurements. Using 2D arbitrary Eulerian-Lagrangian method as well as Baldwin-Lomax turbulent closure model, Sakmann et al. [5-8] and Xue et al. [9-10] investigated comprehensively injector geometry effects on discharge coefficient, liquid film thickness, and spray cone angle of the simplex atomizers. Similar to Chinn and Yule's attempt, Datta and Som [11] predicted theoretically the air core diameter and calculated numerically the discharge coefficient and the spray cone angle with applying two-phase flow solver linked with $k-\varepsilon$ closure model. They reported independently the performance of the pressure-swirl atomizer in a high range of the flow rate. Using the commercial code Fluent 5, Steinthorsson and Lee [12] studied 3D turbulent flow in the pressure-swirl atomizer via Reynolds stress model and VOF model for the air-core formation. After experimental studies in a large scale, Hansen [13] and Madsen et al. [14] simulated

3D flow inside simplex injectors via commercial codes, CFX-4-3 and Fluent 6.1. Different two-phase flow models were applied to predict the axial air core and examined various turbulent models to investigate air core formation. They concluded that the modified laminar flow coupled with VOF model can calculate the axial and tangential velocity along the injector and is more accurately than the turbulent models. Maatje et al. [15-16] emphasized on unsteady behavior and details of liquid and gas flow inside the pressure- swirl atomizer in 2D and 3D numerical calculations. Donjat et al. [17] emphasized on interfacial unsteadiness in rotating core of the atomizer nozzle axis with laminar two-phase flow modeled with VOF method. They concluded the unsteadiness of the air core may be originated from the sheet atomization process. Yeh [18-19] evaluated three- linear eddy viscosity, explicit algebraic Reynolds stress model and differential Reynolds stress model to simulate the pressure-swirl atomizer. His results depicted explicit algebraic Reynolds stress model is more efficient to model the highly swirling flow. Applying the framework of the commercial code Fluent V12.1 using User Defined Functions (UDF), Belhadef et al. [20] studied on both inside and outside of the atomizer via Eulerian-Eulerian two-phase model with Reynolds stress model. They reported that the Sauter mean diameter has some deviation from the experimental results, but the order of magnitude of the velocity components as well as the recirculation zone are comparable with those results. Moghaddam et al. [21] modified the works of Xue [22] and Mandal [23-24] on turbulent flow to investigate non-Newtonian fluid behavior in the pressure- swirl atomizer. Applying the VOF method coupled with $k-\varepsilon$ closure model, they concluded that the spray cone angle decreases and the discharge coefficient increases with increasing power-law index.

The motivation of this work is to simulate the flow field inside the pressure swirl atomizers. For the first time, the topology of the air core formed in the axial zone of the injector is determined by the level set method with capturing of the air-liquid interface. Then, the velocity components and performance of the injector were evaluated. To compare the numerical results of the present work with the experimental data of Horvey [25] and Rizk [26, 27], the laminar and turbulent regime are applied to simulate the flow filed inside the injector. Based on the strongly anisotropy flow, the explicit algebraic Reynolds stress model is also used.

II. Governing Equations

Level Set and Re-initialization Equations: The level set model is used to capture the interface between gas and liquid in a two-phase mixture. Since the interface moves with the velocity of the fluid, the evolution of the interface in a two-dimensional axisymmetric cylindrical coordinate system is governed by the Hamilton-Jacobian equation proposed by Osher et al. [28].

$$\frac{\partial \phi}{\partial t} + u_r \frac{\partial \phi}{\partial r} + u_z \frac{\partial \phi}{\partial z} = 0 \tag{1}$$

$\phi = \phi(r, z, t)$ is the level set function and must be a signed distance function in the computational domain. It is typically a smooth function and represents the shortest normal distance to the interface with the following properties.

$$\phi(\vec{x}, t) = \begin{cases} > 0 & if \ \ \vec{x} \in D_l \\ 0 & if \ \ \vec{x} \ on \ S \\ < 0 & if \ \ \vec{x} \in D_g \end{cases} \tag{2}$$

where $|\phi(\vec{x})| = \min(|\vec{x} - \vec{x}_s|)$ and $\vec{x}_s$ indicated the interface location. $\phi(\vec{x}) > 0$ is related on one side of the interface (high density region) and $\phi(\vec{x}) < 0$ on the other side (low density region). D_l and D_g are liquid and gas domain respectively. S represents the interface between two phases.

By means of simple mixture flow, the properties of the fluid such as density and viscosity are defined respectively as: [29]

$$\rho(\phi) = \rho_l H(\phi) + \rho_g (1 - H(\phi)) \tag{3}$$

$$\mu(\phi) = \mu_l H(\phi) + \mu_g (1 - H(\phi)) \tag{4}$$

To achieve numerical robustness in the computational domain, a smeared out Heaviside function is often used, [29] as:

$$H(\phi) = \begin{cases} 0 & if \ \ \phi < -\varepsilon \\ \frac{1}{2} + \frac{\phi}{2\varepsilon} + \frac{1}{2\pi} \sin\left(\frac{\pi\phi}{\varepsilon}\right) & if \ \ -\varepsilon < \phi < \varepsilon \\ 1 & if \ \ \phi > \varepsilon \end{cases} \tag{5}$$

ε is the thickness of the air-liquid interface. Based on Heaviside function, $\varepsilon = \Delta r / 2$ where Δr is the mesh size in r-direction. For $\varepsilon = 0$, the numerical results will be poor.

In the present work, both liquid and gas flow are determined by the corresponding material properties and no boundary condition is imposed (required) on the interface of two fluids. In addition, the surface tension force can be modelled by applying a volume force coupled with Navier-Stokes equations and the level set model, [29]. One of the main advantages of the level set model is capturing the interface of the two-phase mixture with any complex topology and it may occur at very high turbulent flows. To solve Eq. (1) numerically, the time step should be defined by the stability criterion with respect to viscous and convective terms as follows, [30].

$$\Delta t = \left[\frac{\max\left|u_z^*\right|}{\Delta z^*} + \frac{\max\left|u_r^*\right|}{\Delta r^*} + \frac{4}{\mathrm{Re}}\left(\frac{1}{\Delta z^{*2}} + \frac{1}{\Delta r^{*2}}\right) \right]^{-1} \tag{6}$$

where $u_z^* = u_z / u_0$, $u_r^* = u_r / u_0$, $\Delta z^* = \Delta z / L$ and $\Delta r^* = \Delta r / L$ are normalized parameters. $\mathrm{Re} = L u_f / \nu_f$ is Reynolds number based on the heavy fluid properties,

Solution of Eqs. (?) by marching in time leads to the deviation in mass conservation due to the non-satisfactory of the level set model based on definition of $\nabla \phi = 1$. So, re-initialization equation and its initial condition proposed by Sussman et al. [28] are as follows.

$$\frac{\partial \phi}{\partial \tau} = S\left(\phi_0\right)\left(1 - \sqrt{\phi_r^2 + \phi_z^2}\right) \tag{7}$$

Under the condition of $\phi_0 = \phi\left(\vec{\mathbf{x}}\right)$, $S\left(\phi_0\right)$ is a smoothed function and defined as:

$$S\left(\phi_0\right) = \frac{\phi_0}{\sqrt{\phi_0^2 + \varepsilon^2}} \tag{8}$$

After solution of Eq. (1), the desired signed distance function is obtained by steady state solution of the re-initialization equation.

Navier Stokes equations: Axisymmetric continuity and the Reynolds averaged Navier Stokes equations in the cylindrical coordinate system are, [31].

$$\frac{1}{r}\frac{\partial \rho r u_r}{\partial r}+\frac{\partial \rho u_z}{\partial z}=0 \tag{9}$$

$$\frac{\partial \rho u_r}{\partial t}+\frac{1}{r}\left(\frac{\partial \rho r u_r u_r}{\partial r}+\frac{\partial \rho r u_z u_r}{\partial z}\right)=\frac{1}{r}\frac{\partial}{\partial r}\left(\mu r\frac{\partial u_r}{\partial r}\right)+\frac{1}{r}\frac{\partial}{\partial z}\left(\mu r\frac{\partial u_r}{\partial z}\right)+S_{u_r}+S'_{u_r} \tag{10}$$

$$\frac{\partial \rho u_\theta}{\partial t}+\frac{1}{r}\left(\frac{\partial \rho r u_r u_\theta}{\partial r}+\frac{\partial \rho r u_z u_\theta}{\partial z}\right)=\frac{1}{r}\frac{\partial}{\partial r}\left(\mu r\frac{\partial u_\theta}{\partial r}\right)+\frac{1}{r}\frac{\partial}{\partial z}\left(\mu r\frac{\partial u_\theta}{\partial z}\right)+S_{u_\theta}+S'_{u_\theta} \tag{11}$$

$$\frac{\partial \rho u_z}{\partial t}+\frac{1}{r}\left(\frac{\partial \rho r u_r u_z}{\partial r}+\frac{\partial \rho r u_z u_z}{\partial z}\right)=\frac{1}{r}\frac{\partial}{\partial r}\left(\mu r\frac{\partial u_z}{\partial r}\right)+\frac{1}{r}\frac{\partial}{\partial z}\left(\mu r\frac{\partial u_z}{\partial z}\right)+S_{u_z}+S'_{u_z} \tag{12}$$

where $S_{u_r}, S_{u_\phi}, S_{u_z}$ are laminar source terms and $S'_{u_r}, S'_{u_\theta}, S'_{u_z}$ are turbulent source terms defined respectively as:

$$S_{u_r}=-\frac{\partial p}{\partial r}+\rho\frac{u_\theta^2}{r}+\underbrace{\frac{\partial}{\partial r}\left(\mu\frac{\partial u_r}{\partial r}\right)+\frac{\mu}{r}\frac{\partial u_r}{\partial r}-\mu\frac{u_r}{r^2}+\frac{\partial}{\partial z}\left(\mu\frac{\partial u_z}{\partial r}\right)}_{I}-\mu\frac{u_r}{r^2}+g_r \tag{13}$$

$$S_{u\theta}=-\rho\frac{u_r u_\theta}{r}+\underbrace{\frac{\mu}{r}\frac{\partial u_\theta}{\partial r}-\frac{1}{r}\frac{\partial \mu u_\theta}{\partial r}}_{II}-\mu\frac{u_\theta}{r^2}+g_\theta \tag{14}$$

$$S_{u_z}=-\frac{\partial p}{\partial z}+\underbrace{\frac{\partial}{\partial r}\left(\mu\frac{\partial u_r}{\partial z}\right)+\frac{\mu}{r}\frac{\partial u_r}{\partial z}+\frac{\partial}{\partial z}\left(\mu\frac{\partial u_z}{\partial z}\right)}_{III}+g_z \tag{15}$$

$$S'_{u_r}=\rho\frac{\overline{u'_\theta u'_\theta}}{r}-\frac{1}{r}\left[\frac{\partial}{\partial r}\left(r\rho\,\overline{u'_r u'_r}\right)+\frac{\partial}{\partial z}\left(r\rho\overline{u'_z u'_r}\right)\right] \tag{16}$$

$$S'_{u\theta}=-\rho\frac{\overline{u'_r u'_\theta}}{r}-\frac{1}{r}\left[\frac{\partial}{\partial r}\left(r\rho\,\overline{u'_r u'_\theta}\right)+\frac{\partial}{\partial z}\left(r\rho\overline{u'_z u'_\theta}\right)\right] \tag{17}$$

$$S'_{u_z}=-\frac{1}{r}\left[\frac{\partial}{\partial r}\left(r\rho\,\overline{u'_r u'_z}\right)+\frac{\partial}{\partial z}\left(r\rho\overline{u'_z u'_z}\right)\right] \tag{18}$$

where I, II, and III are zero for incompressible flows and they are not negligible for a two- phase flow with variant molecular properties.

Abandoning the isotropic eddy-viscosity hypothesis, the explicit algebraic Reynolds stress model which is one of the most complex classical turbulence models closes the Reynolds-averaged Navier-Stokes equations by

calculating an explicit term to determine anisotropy Reynolds stress. More details about the applied explicit algebraic Reynolds stress are given in Appendix A.

III. Solution Methodology

Body-fitted Navier-Stokes equations: Since the majority schemes for calculation the level set equation are based on the uniform grid and also the explicit algebraic Reynolds stress model is being more stable in orthogonal-uniform mesh, it is convenient to apply the body-fitted coordinates to transform computational domain to a rectangular one with uniform control volumes. The generalized body-fitted axisymmetric Reynolds averaged Navier-Stokes equations are, [30].

$$\frac{\partial \rho J \Phi}{\partial t}+\frac{1}{r}\frac{\partial \rho r J V^{\,j}\Phi}{\partial q^{j}}=\frac{1}{r}\frac{\partial}{\partial q^{j}}\left(\mu r g^{jk} J \frac{\partial \Phi}{\partial q^{k}}\right)+\left(S_{\Phi}+S'_{\Phi}\right)J \tag{19}$$

where $\Phi=\left[u_r,u_\theta,u_z\right]^T$ and $J=\left(z_\xi r_\eta - z_\eta r_\xi\right)$ is Jacobian. V^j(U,V) is contra variant velocity in which $\mathrm{U}=\left(u_z r_\eta - u_r z_\eta\right)/J$ and $\mathrm{V}=\left(-u_z r_\xi + u_r z_\zeta\right)/J$. g^{jk} is metric tensor and its components are $g^{11}=\left(z_\eta^2+r_\eta^2\right)/J^2$, $g^{12}=g^{21}=-\left(z_\eta z_\xi + r_\eta r_\xi\right)/J^2$ and $g^{11}=\left(z_\xi^2+r_\xi^2\right)/J^2$.

The generalized body fitted the level set equation is defined as:

$$\frac{\partial \phi}{\partial t}+V^{\,j}\frac{\partial \phi}{\partial q^{j}}=0 \tag{20}$$

$q^j\,(\xi,\eta)$ is curvilinear coordinates.

Re-initialization modification is written in the following form.

$$\frac{\partial \phi}{\partial \tau}=S\left(\phi_o\right)\left\{1-\left\{\phi_\xi^2\left[\left(\frac{\partial r}{\partial \eta}\right)^2+\left(\frac{\partial z}{\partial \eta}\right)^2\right]+\phi_\eta^2\left[\left(\frac{\partial r}{\partial \xi}\right)^2+\left(\frac{\partial z}{\partial \xi}\right)^2\right]-2\phi_\xi\phi_\eta\left[\frac{\partial r}{\partial \eta}\frac{\partial r}{\partial \xi}+\frac{\partial z}{\partial \eta}\frac{\partial z}{\partial \xi}\right]\right\}^{0.5}\right\} \tag{21}$$

Level Set Equation Solution: Considering Eq. (20), to keep level set as a signed distance function, it is necessary to accurately discretized spatial and temporal derivatives. In the present work, a 5th order compact upwind finite difference scheme is applied to calculate spatial derivatives.

$$(20-5\lambda)\left.\frac{\partial\phi}{\partial\xi}\right|_{i-1,j}+60\left.\frac{\partial\phi}{\partial\xi}\right|_{i,j}+(20+5\lambda)\left.\frac{\partial\phi}{\partial\xi}\right|_{i+1,j}=$$
$$\frac{1}{h}\left[\left(\frac{-5}{3}+\frac{5}{6}\lambda\right)\phi_{i-2,j}+\left(\frac{-140}{3}+\frac{20}{3}\lambda\right)\phi_{i-1,j}-15\lambda\phi_{i,j}+\left(\frac{140}{3}+\frac{20}{3}\lambda\right)\phi_{i+1,j}+\left(\frac{5}{3}+\frac{5}{6}\lambda\right)\phi_{i+2,j}\right] \tag{22}$$

where $\lambda=-1/12$ is the most optimum value for this free parameter.

The detail derivation of this compact high order upwind finite difference scheme family has been studied by Nouri and Kebriaee [32]. The 4th order Runge Kutta is applied with frozen velocity fields in each time step to march level set equation in time, [33]. To solve re-initialization equation, according to Sussman's method [29], the following equations are introduced.

$$a=D_{\xi}^{-}\phi,\quad b=D_{\xi}^{+}\phi.,\quad c=D_{\eta}^{-}\phi,\quad d=D_{\eta}^{+}\phi \tag{23}$$

Minus superscript of differential operator means applying upwind finite difference scheme as Eq. (21); while downwind scheme in opposite direction of Eq. (22) is applied for plus superscript of differential operator. Also plus and minus superscript related to differential function (i.e. a or b) are defined as,

$$a^{+}\equiv\max(a,0)\qquad b^{-}=-\max(-b,0) \tag{24}$$

ϕ_{ξ} and ϕ_{η} presented in Eq. (20) are calculated with following relations,

$$\phi_{\xi}\equiv f_s\left(a^{+},b^{-}\right)\sqrt{\max\left[(a^{+})^2,(b^{-})^2\right]}$$
$$\phi_{\eta}\equiv f_s\left(c^{+},d^{-}\right)\sqrt{\max\left[(c^{+})^2,(d^{-})^2\right]} \tag{25}$$

where f_s is given by,

$$f_s\left(a^{+},b^{-}\right)=\begin{cases}sign(a) & if\ \max\left[(a^{+})^2,(b^{-})^2\right]=\left(a^{+}\right)^2\\ sign(b) & if\ \max\left[\left(a^{+}\right)^2,\left(b^{-}\right)^2\right]=\left(b^{-}\right)^2\end{cases} \tag{26}$$

Also Based on the problem geometry defined later, the condition of $|\nabla \phi| = 1$ is imposed in the inlet and nozzle wall, [34]. In addition, the level set function is updated by considering the air core diameter over the outlet boundary in each time step.

Reynolds Averaged Navier Stokes Equation Solution: To numerically solve Reynolds averaged Navier Stokes equation, a collocated grid, finite volume based finite difference method is applied. Collocated grid applying the same node for velocity components and pressure calculation can be more convenient for level set equation solution with finite difference scheme. To avoid fluctuation in the collocated grid, Rhie-Chaw's interpolation [35] is put to calculate convection term in discretized equations. Also to improve convergence speed, Pressure Implicit solution by Split Operator method scheme (PISO) proposed by Issa [36] is attached to solve velocity-pressure coupling.

Also first order upwind scheme is applied to discretize RANS equations, [37]. To be more consistent numerical calculation and avoiding superiors flow in two phase flow, pressure gradient, laminar and turbulent source terms are interpolated with cell faces values, [38].

VI. Results and Discussion

Figure (1) represents the schematic of a pressure swirl atomizer, its geometrical parameter and velocity components. In the present work, one experimental case of Horveys' test [25] is applied for validation of numerical solver. The geometry of Horevy's atomizer is defined by swirl chamber length $L_s = 25mm$, diameter $d_s = 50mm$, orifice length $L_o = 20mm$ and orifice diameter $d_o = 10mm.$ In this case, the fluid is fed to the injector via four $20 \times 10\,mm$ rectangular slots. The flow rate is about $2.5 \times 10^{-4}\ m^3/s$ and the Reynolds number of Horvey's case is 18018. The Reynolds number is defined based on the inlet tangential velocity and entrance radius $(= 47\,mm)$. Kinematic viscosity coefficient of liquid is $1.6 \times 10^{-6}\ m^2/s^2$.

To convert the real 3D model of injector to the computational 2-D axisymmetric one, the flow rate of fluid, the inlet angular momentum and the kinetic energy of inlet flow should be fixed as experimental values. So the inlet radial velocity of fluid should be $u_{\theta i} = 0.294\,m/s$ and the tangential component of inlet velocity is $u_{ri} = 0.106\,m/s$.

In addition, the method of Chinn [39] is applied to solve the governing equations of two-phase flow inside the pressure swirl atomizer. In the first step, the single phase Navier-Stokes equations are solved in the whole of

computational domain with the property of liquid phase in the steady state condition. After solving single phase equations, a backward flow is generated along the axis of pressure swirl atomizer. In the second step, the property of gas is replaced in the zone of zero pressure gauge and transient two phase flow equations as well as level set equation are solved inside the injector. The criteria to determine the steady state condition in the computational domain is defined by fixing the core diameter formed in the axial zone of pressure swirl atomizer. e. g. the steady state condition of Horvey's case study was obtained after $t = 1s$ where $dt = 0.0001s$ and the core diameter was fixed after $t = 0.4s$. The maximum error defined by maximum difference of swirl velocity between two successive iterations is also about $e \approx 10^{-7}$ after $t = 1s$.

Figures (2) represent the profile of dimensionless tangential velocity based on inlet tangential velocity in some cross sections of Horvey's injector. In addition, the radial distribution of axial velocity normalized based on inlet tangential velocity along the injector is shown in Figs. (3). As seen, the flow field inside pressure swirl atomizer was calculated for laminar and turbulent flow. As reported by Chinn [39], comparing the experimental results and laminar simulation values shows there is a good agreement between experimental and numerical results, while the turbulent simulation predicts qualitatively the trend of axial and tangential velocities across the injector. These results illustrate the flow in the pressure swirl atomizer of Horvey behaves as a laminar flow in moderately low Reynolds number of 18018.

Three significant functional parameters of every pressure swirl atomizer are diameter of air core, discharge coefficient, and spray cone angle not reported in the Horvey's test, [25]. So Rizk's injector [26, 27] was studied in continue to evaluate the numerical solver in calculation of injector performance.

In the Rizk's case, the liquid water enters from four tangential inlet ports with axial and tangential velocity components into a pressure swirl-atomizer with liquid volume flow rate of $\dot{Q} = 5 \times 10^{-5}\, m^3/s,$ inlet port area $A_p = 10 mm^2,$ swirl chamber length $L_s = 1mm$, diameter $d_s = 8mm$, orifice length $L_o = 4mm$ and orifice diameter $d_o = 2mm.$ The properties of liquid fed into the injector are $\rho = 1000 kg/m^3$ and $\mu = 0.001 kg/ms$ respectively and the gas liquid is air with $\rho = 1 kg/m^3$ and. $\mu = 1 \times 10^{-5} kg/ms$

In order to take into account the effects of 3D inlet ports and satisfaction of mass conservation, kinetic energy and angular momentum, the following inlet velocity components for axisymmetric flow are defined according to the model of Rizk and Lefebvre.

$$u_z = \frac{\dot{Q}}{A_p}, \qquad u_\theta = \frac{\dot{Q}\, r_s}{A_p r} \tag{27}$$

The turbulent intensity and length scale required to the following relationships, assume $I = 0.1$ and $L = 0.00125 d_s$ respectively.

$$k = \frac{3}{2} u_z^2 I^2, \qquad \varepsilon = \frac{k^{1.5}}{L} \tag{28}$$

Due to the emanating liquid bulk into the ambient, the outlet pressure is atmospheric pressure. In addition, the discharge coefficient and spray cone angle are defined as, [11].

$$C_D = \frac{Q}{A_o \sqrt{2\Delta p / \rho_l}} \tag{29}$$

$$\alpha = 2\cos^{-1}\left[\frac{u_{z,o}}{\sqrt{u_{z,o}^2 + u_{\theta,o}^2 + u_{r,o}^2}}\right] \tag{30}$$

where A_o is the outlet area. The mean outlet velocity components can be expressed as:

$$u_{zo} = \frac{4\dot{Q}}{\pi\left(d_o^2 - d_a^2\right)} \tag{31}$$

$$u_{\theta o} = \frac{\int_{r_g}^{r_s} u_\theta u_z \, r\, dr}{\int_{r_g}^{r_s} u_z \, r\, dr} \tag{32}$$

$$u_{ro} = \frac{\int_{r_g}^{r_s} u_r u_z \, r\, dr}{\int_{r_g}^{r_s} u_z \, r\, dr} \tag{33}$$

The mesh independency of flow field is studied for two grid 80×260 and 160×520 for laminar regime flow with reduced velocity $u_{z,i} = 0.25 m/s$. Figures (4a and b) show the distribution of normalized axial and swirl velocity in two cross sections located at $z = 6.13mm$ and $z = 12.56mm$ for two coarse and fine grids, respectively. As shown, the accuracy of coarse grid is sufficient to study the flow filed inside pressure swirl atomizer respect to fine one. Figure (5) represents the grid 80×260 applied in the simulation of flow field inside pressure swirl atomizer. As seen, the mesh grid is refined in the orifice part of injector based on implementation of structural grid and uniformly distributed along the simplex atomizer.

Similar to Horvey's case, laminar and turbulent flow fields are modeled in the pressure swirl atomizer. Table (1) compares the present results with the previous experimental and numerical data. The results show the

implementation of algebraic Reynolds stress as a turbulent closure model improves the prediction of injector performance in comparison of $k-\varepsilon$ closure model in Datta's paper. In addition, there is a very good agreement between the laminar simulation of the present work and the empirical equations. It is worthy to note the simulation of laminar flow in the Horvey's and Rizk's injectors demonstrate the claim of Chinn [38] about to be laminar flow inside the pressure swirl atomizer should be studied more.

Figures (6) illustrate the variation of the air core diameter along the pressure swirl atomizer for laminar and turbulent flow. According to the previous experimental results, the air core diameter in both the swirl chamber and the orifice part are relatively constant while the figures indicate the air core diameter increases in the orifice part. This increment is due to the axial velocity. As reported in Table (1), the diameter of the air core in laminar flow is predicted much more than in the turbulent model. It seems the growth of turbulent eddy viscosity in the turbulent flow field leads to reduce the velocity magnitude and to underestimate the diameter of the air core.

Figures (7a and b) depict the stream lines of turbulent flow in the liquid and air core separately with three swirl vortexes, one near to the inlet, the other one is next to the wall and the third one is located near to the air core. The authors believe that the first one is formed due to the assumption of the 2D inlet conditions while the other two vortexes are produced by high velocity gradient. The streamlines in the air core region are U shape but in the horizontal direction. Because in this region, the velocity is very high and the pressure is very low, then air is drawn into the injector and after traveling a distance turns back to the ambient. The length of the air core depends on the pressure drop in the orifice part. In addition, Figs. (8a and b) show the streamlines of laminar flow in the liquid and air cone zones. Comparing Figs. (7a) and (8a) illustrates the majority of swirl chamber is held by swirling vortexes in laminar flow which leads to increase the axial velocity in the rest of simplex atomizer respect to the turbulent one. The results in Figs. (7b) and (8b) also show high backward velocity in the air core of laminar flow is pushed to the end of swirl chamber while the air flow is trapped in the half of nozzle length in the turbulent flow due to less axial velocity.

Figures (9a-c) illustrate the axial velocity in the cone region as a function of the cone radius. The ordinate axis has been dimensionless by the inlet axial velocity. Figure (9a) belongs to the velocity distribution at the location of $z=0.83mm$ and $r_s=4mm.$ The results of Datta and Som [11] are also reproduced in the figure. There is a bump on the solid line near $r/r_s \simeq 0.8$ and it is attributed to the entrance region effect. This bump will be disappeared when the effect of the entrance region is negligible. Figure (9b) depicts the axial velocity distribution at the location of $z=6.13mm$ and $r_s=1.8mm.$ The solid line near the axis has negative values. It means that there is a reverse flow in this region that belongs to the air core. The agreement between the dashed

line (turbulent flow) and the data of Datta and Som [11] is fairly good in this figure and the previous one. Figure (9c) also reports the velocity distribution at the location of $z = 12.58mm$ and $r_s = 1mm$. In this figure, the region of the reverse flow is more extended with respect to the previous one and also includes completely the air core. The findings in these figures confirm the axial velocity magnitude in laminar flow is predicted much more than turbulent flow either by $k-\varepsilon$ closure model [11] or explicit algebraic Reynolds stress.

Figures (10a-c) demonstrate the tangential velocity distribution of the swirling flow in the cone region as a function of cone radius at the same axial locations of figures (9a-c). In general, the zone close to the axis involving the air core is the region of low swirling flow while the zone close to the wall has high swirl velocity and includes the liquid flow. Figure (10a) is plotted at the location of $z = 0.83mm$ and $r_s = 4mm$. The tangential velocity has been dimensionless by the inlet axial velocity. After a sharp increase in the tangential velocity near the core region, it gradually approaches the inlet axial velocity. This sharp velocity causes a forced vortex is formed in the core region. The highly swirling flow in the laminar flow is seen in Fig. (10a). Figure (10b) exhibits the tangential velocity at the location of $z = 6.13mm$ and $r_s = 1.8mm$. At this location, the most part of the velocity in either [11] or turbulent flow is nearly constant except close to the core region. In the meantime, the disagreement between the turbulent present results and the data of Datta and Som [11] can be originated from different applied turbulent closure models and the constant air core diameter used by Datta and Som [11]. In addition, the free vortex profile in laminar flow is preserved in this location due to the lack artificial eddy viscosity leading to underestimate the tangential velocity. Figure (10c) shows the velocity at the location of $z = 12.56mm$ and $r_s = 1mm$. At this location, the nozzle radius is small, $r_s = 1mm$, and the velocity approaches a maximum value near the nozzle wall. Thus, the forced vortex and no-swirl floe field regimes are dominant in this cross section. The no-swirl velocity is attributed to the backward air flow pushed to the atomizer.

Figures (11a-b) present the radial velocity distribution as a function of radius in the cone region at the locations of $z = 6.13mm$, $r_s = 1.8mm$ and $z = 12.56mm$, $r_s = 1mm$ respectively. The ordinate axis has been dimensionless by the inlet axial velocity and the abscissa axis by the radius of the swirl chamber. There is a transverse flow in both figure, but the radial velocity in laminar regime does not follow its trend in turbulent flow in both Figs. (11a and b). It is seen that the radial velocity has a wavy shape with magnitude about 0.08 times of its corresponding tangential and axial velocity in the previous figures at each cross section of the cone region. Hence, the radial velocity has no significant effect on the performance of the nozzle and its effect can be neglected in the solution analysis.

Figures (12a-b) show the turbulent kinetic energy as a function of radius in the cone region at the locations of $z = 6.13mm$, $r_s = 1.8mm$ and $z = 12.56mm$, $r_s = 1mm$ respectively. The intensity of the kinetic energy increases drastically near the interface between the air core and the water liquid. The comparison between two figures also shows that the maximum of the turbulent kinetic energy increases as the flow approaches the nozzle outlet, i.e., when the fluid flows from $z = 6.13mm$ to $12.58mm$.

To be deeper in evaluation of flow field inside the pressure swirl-atomizer, the sensitivity of injector performance is studied as a function of gas-liquid interface thickness in laminar flow. The findings show the variation of interface thickness ε has no significant affect on the air core diameter, while the spray cone angle increases slightly with growth of axial velocity due to reducing the average density across the outlet. Regardless of liquid region, the zone of air core is so sensitive to the interface thickness due to high density ratio between liquid and gas fluids. Figures (13) represent the distribution of normalized axial velocity for $\varepsilon = \Delta r / 2$ and $\varepsilon = 3\Delta r / 2$. As shown, the magnitude of axial velocity in the backward zone of air core increases and effect of high viscosity coefficient ration of two fluids has diffused in each phase.

Conclusions

The Reynolds averaged Navier-Stokes equation coupled with Reynolds stress model as well as the level set equation are solved by finite volume based on finite difference method to simulate the air-water two-phase flow inside the pressure swirl atomizer. The high order compact upwind finite difference method with re-initialization equation being used to capture the interface between the air core and the liquid water with decreasing the mass conservation error in the level set equation. Converting Rankin vortex from the swirl chamber to forced vortex in orifice part can be predicted by this model. The proposal model shows a considerable improvement in the results so that the values of the discharge coefficient, film thickness, and spray cone angle are satisfactory with the previous experimental results and the error is less than 10 percent.

Appendix A- Turbulence Modeling

Explicit Algebraic Reynolds Stress Model: Use of the Reynolds stress model is a must when the flow features of interest are the result of anisotropy in the Reynolds stress, but it is the most elaborate model. Among the examples is highly swirling flow. Alternative the Reynolds stress model is the algebraic stress model which is an economical way of accounting for the anisotropy of Reynolds stresses without going to the full length of solving the Reynolds stress transport equations. The initial idea in algebraic Reynolds stress model is neglecting or modeling the convective and diffusive transport terms of the Reynolds stress anisotropy defined by $a_{ij} = \overline{u_i' u_j'}/k - 2\delta_{ij}/3$. Modeling pressure-strain via the Reynolds stress anisotropy and dissipation tensor via the mean velocity gradient then inserting the results in Reynolds stress anisotropy transport equation, an implicit algebraic Reynolds stress tensor equation are obtained, [43-45].

$$\left(c_1 - 1 + \frac{\mathrm{P}}{\varepsilon}\right)\mathbf{a} = -\frac{8}{15}\mathbf{S} + \frac{7c_2+1}{11}\left(\mathbf{a\Omega} - \mathbf{\Omega a}\right) - \frac{5-9c_2}{11}\left(\mathbf{aS} + \mathbf{Sa} - \frac{2}{3}tr\left\{\mathbf{aS}\right\}\mathbf{I}\right) \tag{A1}$$

$c_1 = 1.8$ and $c_2 = 5/9.$ $\mathbf{I}$ is the identity matrix and the product of two matrices is defined as $\left(\mathbf{AB}\right)_{ij} = A_{ik}B_{kj}$ and $tr\{\ \}$ denotes the trace. $\mathbf{S}$ and $\mathbf{\Omega}$ are defined as mean strain and mean rotation tensor normalized with the turbulent timescale, respectively.

$$S_{ij} = \frac{\tau}{2}\left(\nabla u_{ij} + \nabla^T u_{ji}\right)$$
$$\Omega_{ij} = \frac{\tau}{2}\left(\nabla u_{ij} - \nabla^T u_{ji}\right) \tag{A2}$$

The velocity gradient components in cylindrical coordinate are given in appendix B. To limit turbulent time scale with Kolmogorov's time scale, τ is defined by

$$\tau = \max\left[\frac{k}{\varepsilon}, C_\tau\sqrt{\frac{\nu}{\varepsilon}}\right] \tag{A3}$$

where k and ε are turbulent kinetics energy and dissipation rate, respectively. $C_\tau = 6.0$ is a constant.

Neglecting the diffusion and damping terms in Eq. (A1), the numerical solution of the implicit algebraic Reynolds stress equation is found abstruse and arduous. So explicit algebraic Reynolds stress equation is introduced by applying Caley–Hamilton theorem as,

$$\mathbf{a} = f_1\beta_1\mathbf{S} + \frac{(3B_2-4)\left(1-f_1^{\,2}\right)}{\max\left(II_S, II_S^{eq}\right)}\left[\mathbf{S}^2 - \frac{1}{3}II_S\mathbf{I}\right] + f_1^{\,2}\beta_3\left[\mathbf{\Omega}^2 - \frac{1}{3}II_\Omega\mathbf{I}\right] +$$
$$\left[f_1^{\,2}\beta_4 - \frac{B_2\left(1-f_1^{\,2}\right)}{2\max\left(II_S, II_S^{eq}\right)}\right](\mathbf{S\Omega}-\mathbf{\Omega S}) + f_1\beta_6\left[\mathbf{S\Omega}^2 + \mathbf{\Omega}^2\mathbf{S} - \frac{2}{3}IV\ \mathbf{I}\right] + f_1^{\,2}\beta_9\left(\mathbf{\Omega S\Omega}^2 - \mathbf{\Omega}^2\mathbf{S\Omega}\right) \tag{A4}$$

where near wall effect in the explicit algebraic Reynolds stress equation has been appeared in damping function f_1 defined as follows,

$$f_1 = 1 - \exp\left(C'_{y1}\sqrt{\mathrm{Re}_y} - C'_{y2}\,\mathrm{Re}_y^2\right) \tag{A5}$$

$C'_{y1} = 2.4/26$, $C'_{y2} = 0.003/26$, and $\mathrm{Re}_y = \sqrt{k}\,y_n/\nu$.

In Eq. (A4), good fit to accurate data is obtained by choosing $B_2 = 1.8$ and II_S^{eq}, $\mathrm{P} = \varepsilon$ and $II_S^{eq} = 405c_1^2/216c_1 - 160$ is the equilibrium value. For general 3-D flows, the independent groups of β-coefficients can be written as functions of the five independent invariants of $\mathbf{S}$ and $\mathbf{\Omega}$,

$$\beta_1 = -\frac{N\left(2N^2 - 7II_\Omega\right)}{Q} \quad \beta_3 = -\frac{12N^{-1}IV}{Q}, \quad \beta_4 = -\frac{2\left(N^2 - 2II_\Omega\right)}{Q} \quad \beta_6 = -\frac{6N}{Q} \quad \beta_9 = \frac{6}{Q} \tag{A6}$$

The dominator Q is given by

$$Q = \frac{5}{6}\left(N^2 - 2II_\Omega\right)\left(2N^2 - II_\Omega\right) \tag{A7}$$

N is $\mathbf{a}$ coefficient in the implicit algebraic Reynolds stress equation and calculated for general 3-D flows by

$$N = N_c + \frac{162\left(\varphi_1 + \varphi_2 N_c^{\,2}\right)}{D} \tag{A8}$$

$$D = 20N_c^{\,4}\left(N_c - \frac{c'_1}{2}\right) - II_\Omega\left(10N_c^{\,3} + 15c'_1N_c^{\,2}\right) + 10c'_1II_\Omega^{\,2} \tag{A9}$$

$\varphi_1 = IV^2$ and $\varphi_2 = V^2 - II_S II_\Omega / 2$ and for 2-D flows, N_c is given by

$$N_c = \begin{cases} \frac{c_1'}{3} + \left(P_1 + \sqrt{P_2}\right)^{1/3} + sign\left(P_1 - \sqrt{P_2}\right)\left|P_1 - \sqrt{P_2}\right|^{1/3} & P_2 \geq 0 \\ \frac{c_1'}{3} + 2\left(P_1^2 - P_2\right)^{1/6} \cos\left[\frac{1}{3}\cos^{-1}\left(\frac{P_1}{\sqrt{P_1^2 - P_2}}\right)\right] & P_2 < 0 \end{cases} \tag{A10}$$

and

$$P_1 = \left(\frac{c_1'^2}{27} + \frac{9}{20} II_S - \frac{2}{3} II_\Omega\right) c_1', \qquad P_2 = P_1^2 - \left(\frac{c_1'^2}{9} + \frac{9}{10} II_S + \frac{2}{3} II_\Omega\right)^3 \tag{A11}$$

With modification of model behavior in regions having small production to dissipation ratio, the definition of c_1' -coefficient reads

$$c_1' = \frac{9}{4}\left(c_1 - 1 + C_D \max\left[1 + \beta_1^{eq} II_S, 0\right]\right) \tag{A12}$$

where $C_D = 2.2$ and β_1^{eq} is defined as,

$$\beta_1^{eq} = -\frac{6}{5}\frac{N^{eq}}{\left(N^{eq}\right)^2 - 2II_\Omega}, \qquad N^{eq} = \frac{9c_1}{4} \tag{A13}$$

and the invariant of $\mathbf{S}$ and $\mathbf{\Omega}$ tensors are defined by,

$$II_S = tr\left\{\mathbf{S}^2\right\}, \quad II_\Omega = tr\left\{\mathbf{\Omega}^2\right\}, \quad IV = tr\left\{\mathbf{S}\mathbf{\Omega}^2\right\}, \quad V = tr\left\{\mathbf{S}^2\mathbf{\Omega}^2\right\} \tag{A14}$$

Low Reynolds model for $k-\varepsilon$ Equation: To calculate the turbulent kinetic energy and the dissipation rate, Chien's low Reynolds model of $k-\varepsilon$ is applied as follows, [46].

$$\frac{\partial \rho \mathrm{K}}{\partial t} + \frac{1}{r}\left(\frac{\partial \rho r u_r \mathrm{K}}{\partial r} + \frac{\partial \rho r u_z \mathrm{K}}{\partial z}\right) = \frac{\partial}{\partial r}\left(\left(\mu + \mu_t\right)\frac{\partial \mathrm{K}}{\partial r}\right) + \frac{\partial}{\partial z}\left(\left(\mu + \mu_t\right)\frac{\partial \mathrm{K}}{\partial z}\right) + \mathrm{P} - \varepsilon \tag{A15}$$

$$\frac{\partial \rho \bar{\varepsilon}}{\partial t} + \frac{1}{r}\left(\frac{\partial \rho r u_r \bar{\varepsilon}}{\partial r} + \frac{\partial \rho r u_z \bar{\varepsilon}}{\partial z}\right) = \frac{\partial}{\partial r}\left[\left(\mu + \mu_t\right)\frac{\partial \bar{\varepsilon}}{\partial r}\right] + \frac{\partial}{\partial z}\left[\left(\mu + \mu_t\right)\frac{\partial \bar{\varepsilon}}{\partial z}\right] + C_{\varepsilon 1}\mathrm{P}\frac{\bar{\varepsilon}}{\mathrm{K}} - f_2 C_{\varepsilon 2}\mathrm{P}\frac{\bar{\varepsilon}^2}{\mathrm{K}} + E \tag{A16}$$

where turbulent viscosity is defined by $\mu_t = C_\mu^{eff} f_\mu \rho \mathrm{K} \tau$ and C_μ^{eff} is given by,

$$C_\mu^{eff} = -\frac{1}{2} f_1 \left(\beta_1 + II_\Omega \beta_6 \right) \tag{A17}$$

and turbulent dissipation rate reads

$$\varepsilon = \overline{\varepsilon} + D \tag{A18}$$

Turbulent kinetic energy production appeared in k and ε equations can be calculated explicitly via Reynolds stress and mean gradient velocity as,

$$\mathrm{P} = \overline{u_i' u_j'} u_{i,j} \tag{A19}$$

$C_{\varepsilon 1}$, $C_{\varepsilon 2}$, σ_k pick standard value [47] and some other coefficients in $k-\varepsilon$ equation are listed in table B1.

Appendix B- Velocity Gradient Components in the Cylindrical Coordinate

$$u_{rr} = \frac{\partial u_r}{\partial r}, \quad u_{\theta\theta} = \frac{1}{r}\left(\frac{\partial u_\theta}{\partial \theta} + u_r \right), \quad u_{zz} = \frac{\partial u_z}{\partial z}$$
$$u_{rz} = \frac{\partial u_r}{\partial z}, \quad u_{zr} = \frac{\partial u_z}{\partial r} \quad u_{r\theta} = \frac{1}{r}\frac{\partial u_r}{\partial \theta}, \quad u_{\theta r} = \frac{\partial u_\theta}{\partial r} - \frac{u_\theta}{r} \quad u_{z\theta} = \frac{1}{r}\frac{\partial u_z}{\partial \theta}, \quad u_{z,r} = \frac{\partial u_\theta}{\partial z} \tag{B-1}$$

References

[1] Kim, S., Khil, T., Kim, D., and Yoon, Y., "Effect of Geometric Parameters on the Liquid Film Thickness and Air Core Formation in a Swirl Injector", *Measurement Science and Technology*, Published online 11 Dec. 2008, Vol. 20, No. 1, 2009, pp. 015403.

doi: 10.1088/0957-0233

[2] Chinn, J.J., Yule, A.J., and De Keukelaere, H. J. K., "Swirl Atomizer Internal Flow: A Computational and Experimental Study", 12th Annual Conference of *ILASS*-Europe, Lund, Sweden, June 1996, pp. 41-46.

[3] Cooper, D., Chinn, J.J., and Yule, A. J., "Experimental Measurements and Computational Predictions of the Internal Flow Field in Pressure Swirl Atomizer", *Proceedings of the 15th International Conference on Liquid Atomisation and Spray Systems: ILASS-Europe-1999*, ONERA, Toulouse, July 1999.

[4] Yule, A.J., and Chinn, J.J., "The Internal Flow and Exit Conditions of Pressure Swirl Atomizers", *Atomization and Sprays*, Vol. 10, Issue 2, 2000, pp. 121-146.

[5] Sakman, A.T., Jog, M.A., Jeng, S.M., and Benjamin, M.A., "A Numerical Parametric Study of Simplex Fuel Nozzle Internal Flow and Performance", *34th AIAA/ASME/SAE/ASEE Joint Propulsion Conference & Exhibit*, Cleveland, Ohio, July 1998, AIAA Paper 98-3906.

[6] Jeng, S.M., Jog, M.A., and Benjamin, M.A., "Computational and Experimental Study of Liquid Sheet Emanating from Simplex Fuel Nozzle", *AIAA Journal*, Vol. 36, Issue 2, 1998, pp. 201-207.
doi: 10.2514/2.7502.

[7] Liao, Y., Sakman, A.T., Jeng, S.M., Jog, M.A., and Benjamin, M.A., "A Comprehensive Model to Predict Simplex Atomizer Performance", *Journal of Engineering for Gas Turbines and Power*, Vol. 121, Issue 2, April 1999, pp. 285-294.
doi:10.1115/1.2817119

[8] Sakman, A.T., Jog, M.A., Jeng, S.M., and Benjamin, M.A., "Parametric Study of Simplex Fuel Nozzle Internal Flow and Performance", *AIAA Journal*, Vol. 38, 2000, pp. 1214-1218.
doi: 10.2514/2.1090

[9] Xue, J., Jog, M. A., Jeng, S. M., Steinthorsson, E., and Benjamin, M. A., "Computational Model to Predict Flow in Simplex Fuel Atomizer", *38th AIAA/ASME/SAE/ASEE Joint Propulsion Conference & Exhibit*, Indianapolis, Indiana, July 2002, AIAA paper 2002-3710.

[10] Xue, J., Jog, M. A., Jeng, S. M., Steinthorsson, E., and Benjamin, M. A., "Effect of Geometric Parameters on Simplex Atomizer Performance", *AIAA Journal*, Vol. 42, Issue. 12, Dec. 2004, pp. 2408-2415.
doi: 10.2514/1.2983

[11] Datta, A., and Som, S.K., "Numerical Prediction of Air Core Diameter, Coefficient of Discharge and Spray Cone Angle of a Swirl Spray Pressure Nozzle", *International Journal of Heat and Fluid Flow*, Vol. 21, Issue. 4, August 2000, pp. 412-419.
doi: 10.1016/S0142

[12] Steinthorsson, E., and Lee, D. M., "Numerical Simulations of Internal Flow in a Simplex Atomizer", *Proceedings of the Eighth International Conference on Liquid Atomization and Spray Systems: ICLASS-2000*, Pasadena, CA, July 2000, pp. 324-331.

[13] Hansen, K. G., Madsen, J., Trinh, C. M., Ibsen, C. H., Solberg, T., and Hjertager, B. H., "A Computational and Experimental Study of the Internal Flow in Scaled Pressure-Swirl Atomizer", *18th Annual Conference on Liquid Atomization & Spray Systems: ILASS-Europe 2002*, Zaragoza, Spain, September 2002.

[14] Madsen, J., Hjertager, B. H., and Solberg, T., "Numerical Simulation of Internal Flow in a Large-Scale Pressure-Swirl Atomizer", *18th Annual Conference on Liquid Atomization & Spray Systems: ILASS-Europe 2004*, Nottingham, England, September 2004.

[15] Maatje, U., Von Lavante, E., and Albina, F. A., "Numerical Simulation of Unsteady Effects in Simplex Nozzles", *32nd AIAA Fluid Dynamics Conference and Exhibit*, St. Louise, USA, June 2002, AIAA paper 2002-3179.

[16] Lavante, E. von, Maatje, U., and Albina, F.O., "Investigation of Unsteady Effects in Pressure Swirl Atomizers", *18th Annual Conference on Liquid Atomization & Spray Systems: ILASS-Europe 2002*, Zaragoza, Spain, September 2002.

[17] Donjat, D., Estivalezes, J. L., and Michau, M., "A Description of the Pressure Swirl Atomizer Internal Flow", *ASME 2002 Joint U.S.-European Fluids Engineering Division Conference: FEDSM2002*, Montreal, Quebec, Canada, Volume 1: Fora, Parts A and B, July 2002, pp. 439-444.

[18] Yeh, C. L., "Numerical Simulation of a Turbulent Liquid Jet Emanating from a Plain-Orifice Atomizer and a Pressure-Swirl Atomizer", *Numerical Heat Transfer, Part A*, Vol. 51, Issue. 12, 2007, pp. 1187–1212.

doi: 10.1080/10407780601009082

[19] Yeh, C. L., "Turbulent Flow Simulation of Liquid Jet Emanating from Pressure-Swirl Atomizer", *Heat and Mass Transfer,* Vol. 44, Issue. 3, 2008, pp. 275–280.

doi: 10.1007/s00231-007-0237-8

[20] Belhadef, A., Vallet, A. , and Anselmet, F., “Pressure-Swirl Atomization Modelling Using the Eulerian Approach”, 23rd annual conference on Liquid Atomization and Spray Systems: ILASS-Europe-2010, Brno, Czech Republic, September 2010.

[21] Moghaddam, M. R., Elahi, R., Razavi, M. R. M., and Ayani, M. B., “Modeling of Non-Newtonian Fluid Flow within Simplex Atomizers”, ASME 2010 10th Biennial Conference on Engineering Systems Design and Analysis, Vol. 3, Istanbul, Turkey, July 2010, pp. 549-556.

doi:10.1115/ESDA2010-25266.

[22] Xue, J., “Computational Simulation of Flow Inside Pressure-Swirl Atomizers”, Ph.D. Dissertation, Department of Mechanical, Industrial and Nuclear Engineering, University of Cincinnati, Cincinnati, Ohio, 2001.

[23] Mandal, A., “Computational Modeling of Non Newtonian Fluid Flow in Simplex Atomizers”, M.Sc. Dissertation, Department of Mechanical Engineering, University of Cincinnati, Cincinnati, Ohio, 2007.

[24] Mandal, A., Jog, M.A., Xue, J., and Ibrahim, A.A., “Flow of Power-Law Fluids in Simplex Atomizers”, *International Journal of Heat and Fluid Flow,* Vol. 29, Issue. 5, October 2008, pp. 1494–1503.

doi:10.1016/j.ijheatfluidflow.2008.05.006

[25] Horvey, M., Leuckel, W., “Experimentall and Theoritical Investigation of Swirl Nozzles for Pressure Jet Atomization”, *German Chemical Engineering Journal* , Vol. 9, 1986, pp. 276-283.

doi: 0343-5539/86/0510-0276

[26] Rizk, N. K., and Lefebvre, A. H., “Internal Flow Characteristics of Simplex Swirl Atomizers”, *AIAA Journal of Propulsion and Power,* Vol. 1, Issue. 3, May 1985, pp. 193-199.

[27] Rizk, N. K., and Lefebvre, A. H., “Prediction of Velocity Coefficient and Spray Cone Angle for Simplex Swirl Atomizers”, *Proceedings of the Third International Conference on Liquid Atomisation and Spray Systems: ICLASS*-85, London, England, Vol. 1(A87-13826 03-34), July 1985, p. III C/2/1-16.

[28] Osher, S., and Fedkiw, R., “Level Set Methods and Dynamic Implicit Surfaces”, Applied Mathematical Sciences, 1st ed., Vol. 153, Springer-Verlag, New York, 2003.

[29] Sussman, M., Smereka, P., and Osher, S., “A Level Set Approach for Computing Solutions to Incompressible Two-Phase Flow”, *Journal of Computational Physics*, Vol. 114, Issue 1, 1994, pp. 146–159.

doi: 10.1006/jcph.1994.1155

[30] Olsson , E., Kreiss, G., “A conservative level set method for two phase flow”, *Journal of Computational Physics*, Vol. 210, 2005, pp. 225–246

doi:10.1016/j.jcp.2005.04.007

[31] Ferziger, J. H., and Peric, M., “Computational Methods for Fluid Dynamics”, 3rd ed., Springer-Verlag, Berlin, 2002.

[32] Borujerdi, A. N., and Kebriaee, A., “Upwind Compact and Explicit High Order Finite difference Schemes for Level Set Technique”, *International Journal for Computational Methods in Engineering Science & Mechanics,*Vol. x, pp xx-xx, 2011. (Accepted),

[33] Süli, E., and Mayers, D. F., “An Introduction to Numerical Analysis”, Cambridge University Press, 1st ed., 2003.

[34] Christafakis, A., Alexopoulos. J., Tsangaris, S., “Modelling of two-phase incompressible flows in ducts”, *Applied Mathematical Modelling* **33**, 2009, pp. 1201–1212.

doi:10.1016/j.apm.2008.01.014.

[35] Rhie, C. M., and Chow, W. L., “Numerical Study of Turbulent Flow Past an Airfoil with Trailing Edge Separation”, *AIAA Journal*, Vol. 21, Issue. 11, 1983, pp. 1525-1532.

doi: 10.2514/3.8284

[36] Issa, R. I., “Solution of the Implicitly Discretized Fluid Flow Equation by Operator Splitting”, *Journal of Computational Physics*, Vol. **62**, Issue. 1, Jan. 1986, pp. 40-65.

doi:10.1016/0021-9991(86)90099-9

[37] Versteeg, H. K., and Malalaskera, W., “An Introduction to Computational Fluid Dynamics”, 2nd ed., Pearson Education Ltd, 2007.

[38] Montazeri, H., “A Consistent Numerical Method for Simulating Interfacial Turbulent Flows”, Ph. D. Dissertation, Department of Mechanical and Industrial Engineering, University of Toronto, Toronto, Canada, 2010.

[39] Dgdklg

[40] sfhaskjf

[41] Taylor, G. I., "The Mechanics of Swirl Atomizers", *Proceedings of the Seventh International Congress for Applied Mechanics,* Vol. 2, Pt. 1, 1948, pp. 280-285.

[42] Suyari, M., and Lefebvre, A. H., "Film Thickness Measurements in a Simplex Swirl Atomizers", *AIAA Journal of Propulsion and Power*, Vol. 2, No. 6, Nov. 1986, pp. 528-533.

[43] Jones, A. R., "Design Optimization of a Large Pressure Jet Atomizer for Power Plant", *Proceedings of the Second International Conference on Liquid Atomization and Spray Systems*, Madison, Wis., 1992, pp. 181-185.

[44] Wallin, S., "Engineering Turbulence Modelling for CFD with a Focus on Explicit Algebraic Reynolds Stress Models", Ph. D. Dissertation, Department of Mechanics, Royal Institute of Technology, Stockholm, Sweden, 2000.

[45] Wallin, S., and Johansson, A. V., "An Explicit Algebraic Reynolds Stress Model for Incompressible and Compressible Turbulent Flows", *Journal of Fluid Mechanics*, Vol. 403, 2000, pp. 89-132.

[46] Yun, A., "Development and Analysis of Advanced Explicit Algebraic Turbulence and Scalar Flux Models for Complex Engineering Configurations", Ph. D. Dissertation, Department of Energy and Power Plant, der Technischen Universität Darmstadt, Germany, 2005.

[47] Chien, K. Y., "Predictions of Channel and Boundary-Layer Flows with a Low-Reynolds Number Turbulence Model", *AIAA Journal*, Vol. 20, Issue. 1, 1982, pp. 33-38.

doi: 10.2514/3.51043

[48] Jones, W. P., and Launder, B. E., "The Prediction of Laminarization with a Two-Equation Model of Turbulence", *International Journal of Heat and Mass Transfer*, Vol. 15, Issue. 2, Feb. 1972, pp. 301-314.

doi: 10.1016/0017-9310(72)90076-2

Table 1 Comparison of air core diameter, discharge coefficient, and spray cone angle

Author	type of data	d_{air}/d_o	C_D	θ
present work (laminar flow)	numerical	0.70	0.388	68.22
present work (turbulent flow)	numerical	0.64	0.428	71.23
Datta [11]	numerical	0.45	0.448	74.30
Taylor [39]	analytical	0.632	---	---
Rizk [26]	experimental	0.59	0.39	---
Rizk [26]	experimental	---	---	69.63
Suyari [40]	experimental	0.697	---	---
Jones [41]	experimental	---	0.382	---

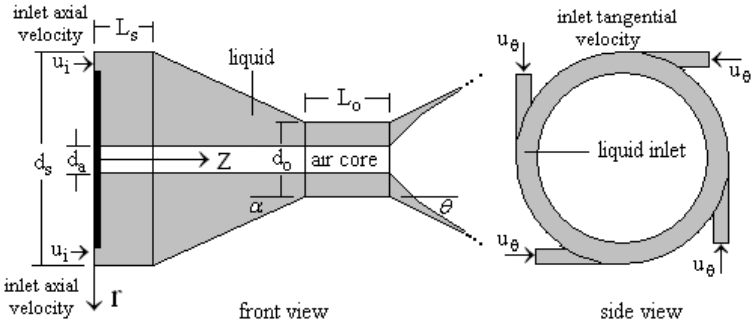

Fig. 1 schematic of a pressure swirl atomizer nozzle

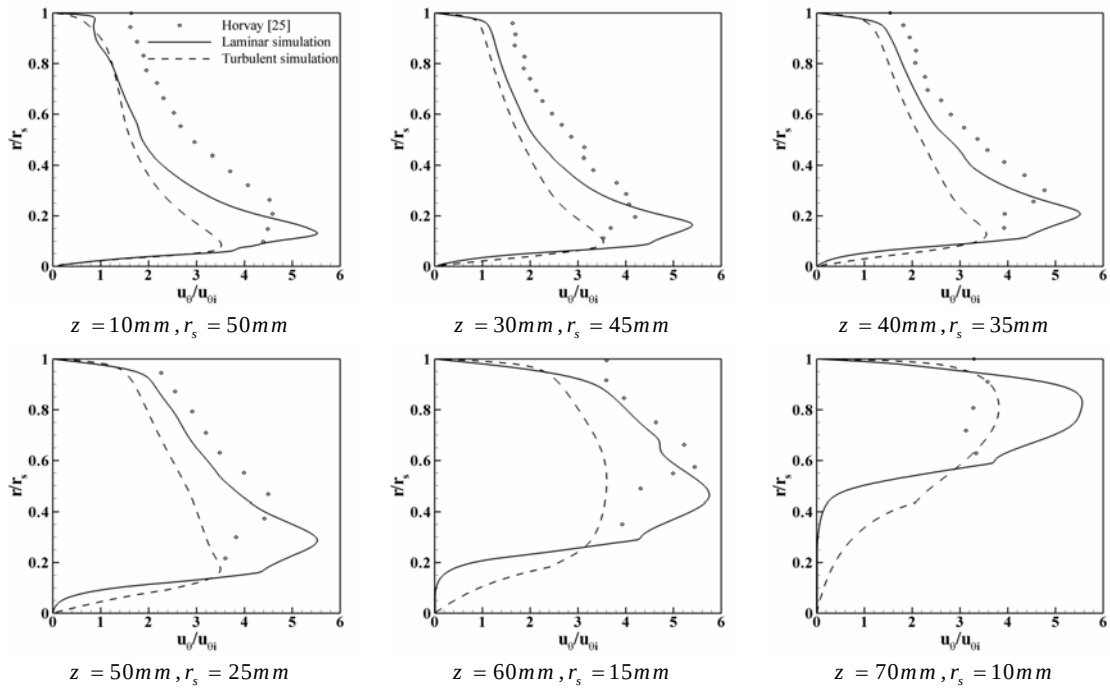

Fig. 2 tangential velocity profile across the cross section of Horvey's injector along the nozzle

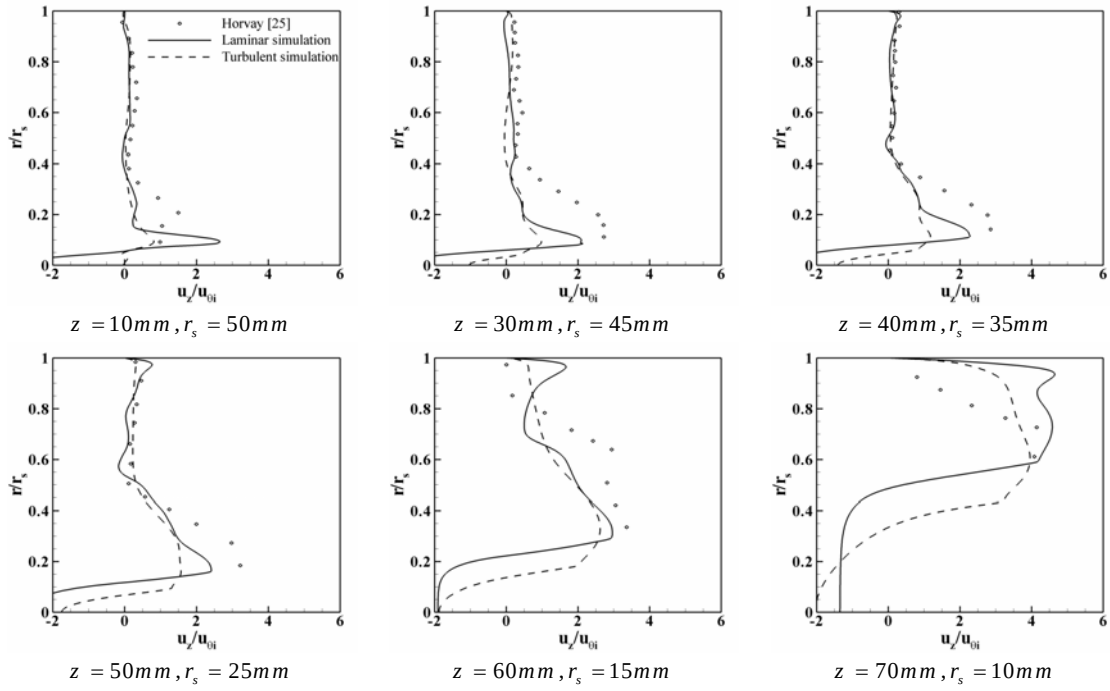

Fig. 3 axial velocity profile across the cross section of Horvey's injector along the nozzle

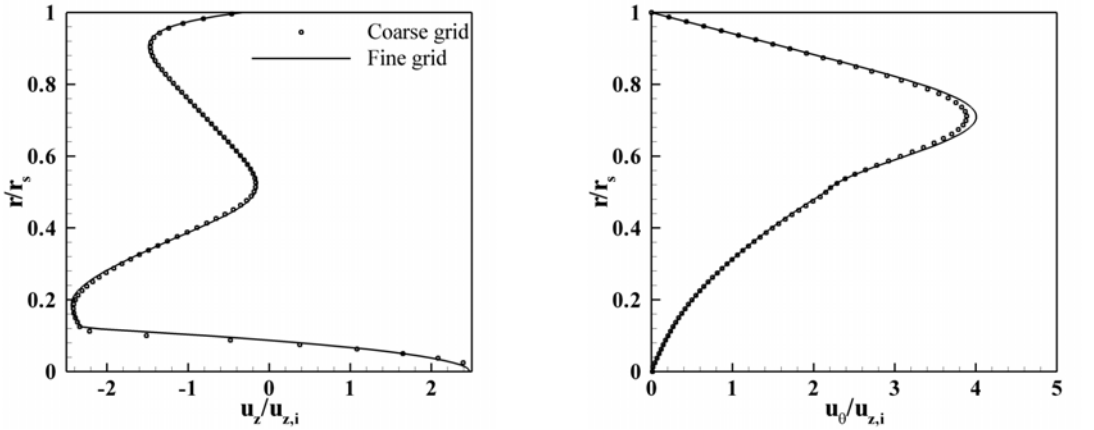

(a) axial velocity for $z = 6.13mm$ and $r_s = 1.8mm$

(a) tangential velocity for $z = 12.56mm$ and $r_s = 1mm$

Fig. 4 mesh independency study between fine and coarse grid

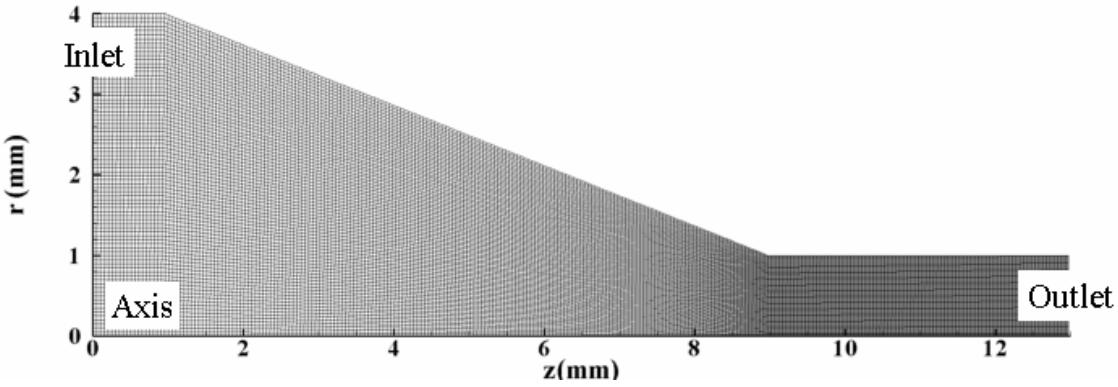

Fig. 5 Structural grid applied as computational domain, 80×260 number of cells

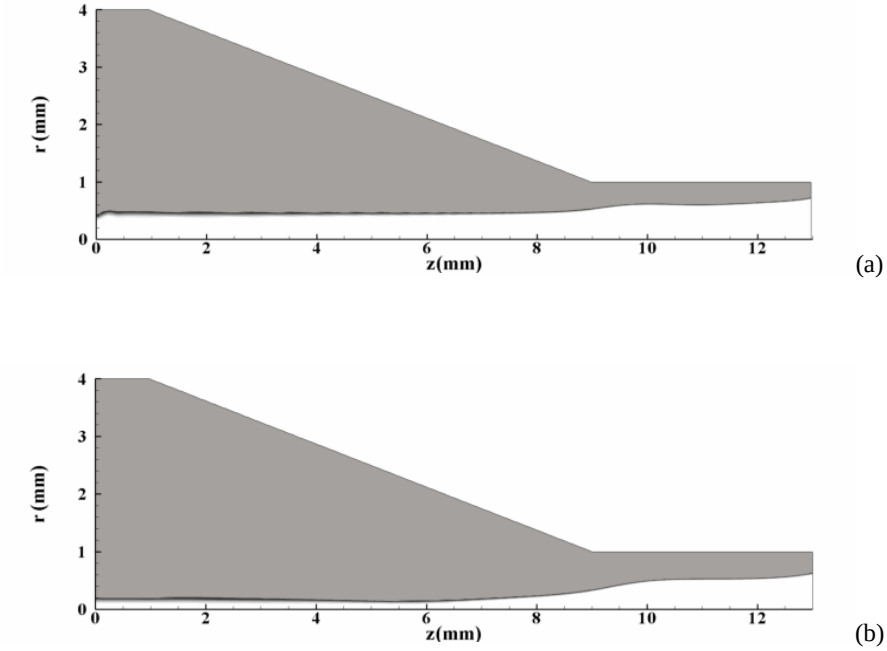

Fig. 6 Air core diameter along the nozzle, (a) laminar flow (b) turbulent flow

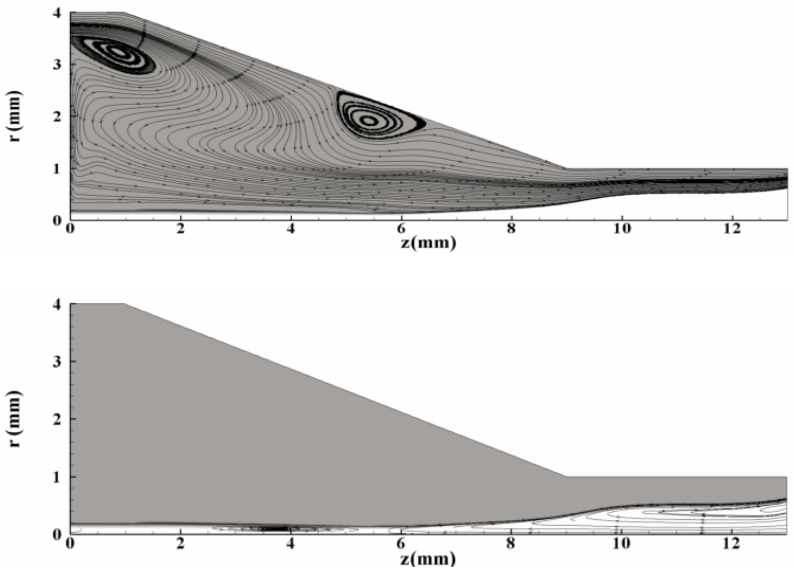

(a)

(b)

Fig. 7 stream lines of turbulent flow (a) in the liquid zone (b) in the air core

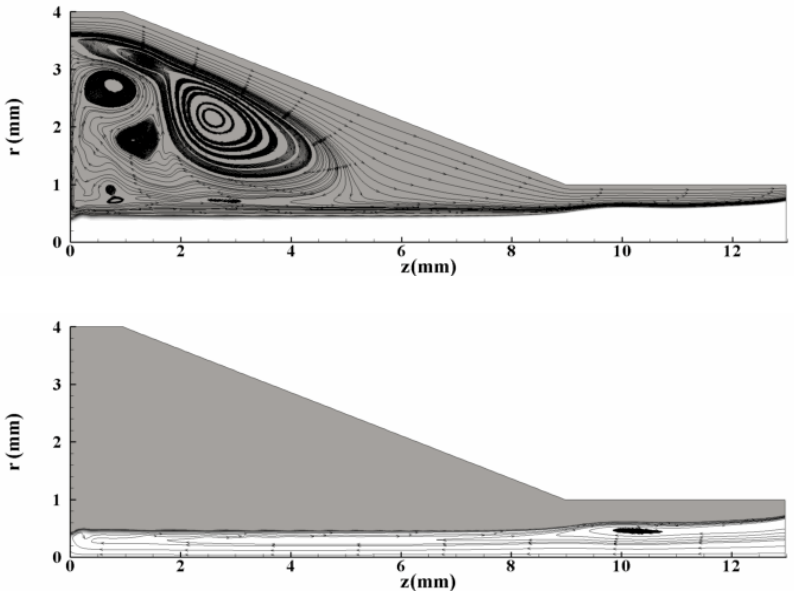

(a)

(b)

Fig. 8 stream lines of laminar flow (a) in the liquid zone (b) in the air core

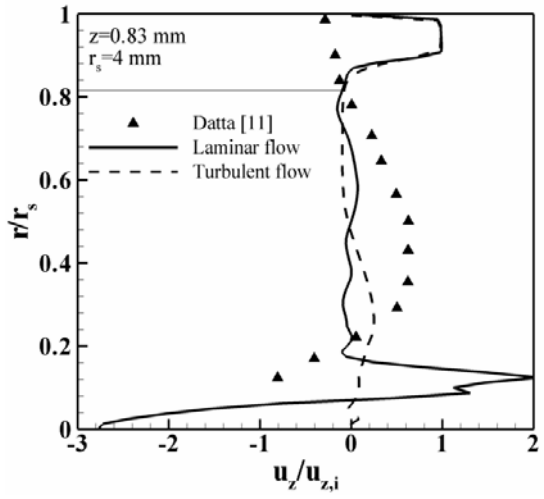

(9a)

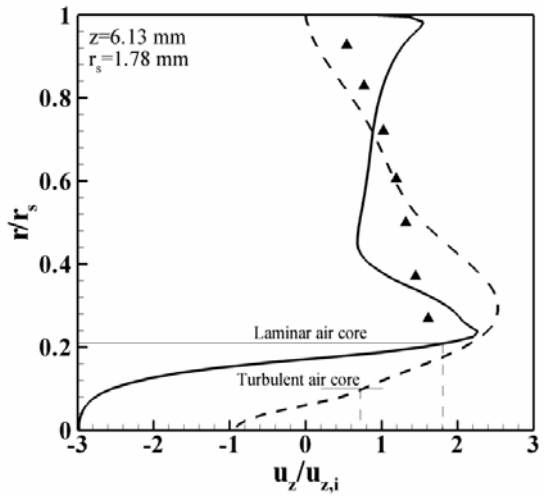

(9b)

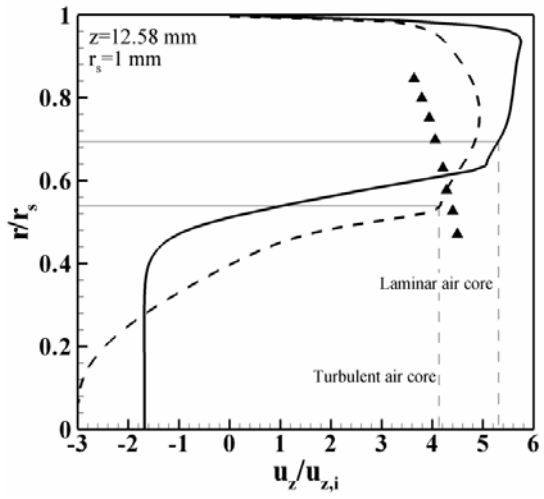

(9c)

Fig. 9 Axial velocity across the cone region at different axial locations of the nozzle

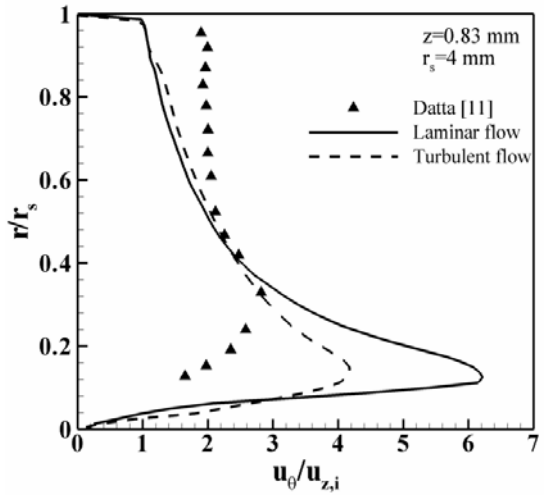

(10a)

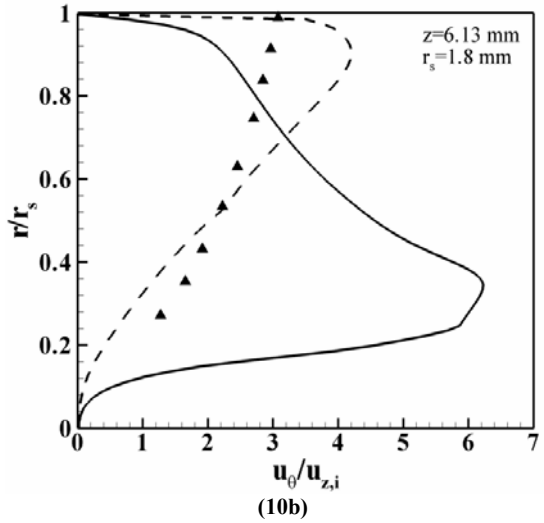

(10b)

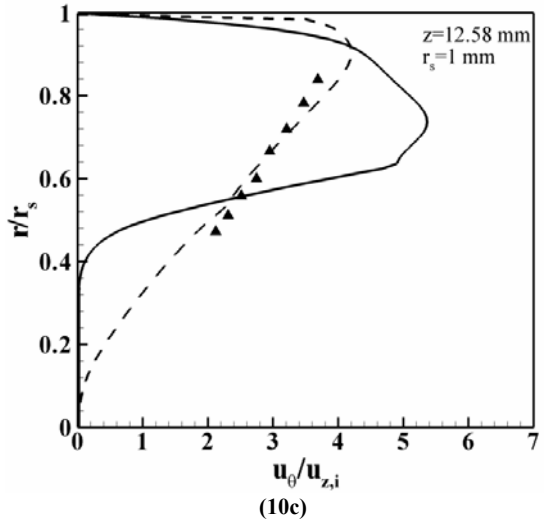

(10c)

Fig. 10 Tangential velocity across the cone region at different axial locations of the nozzle

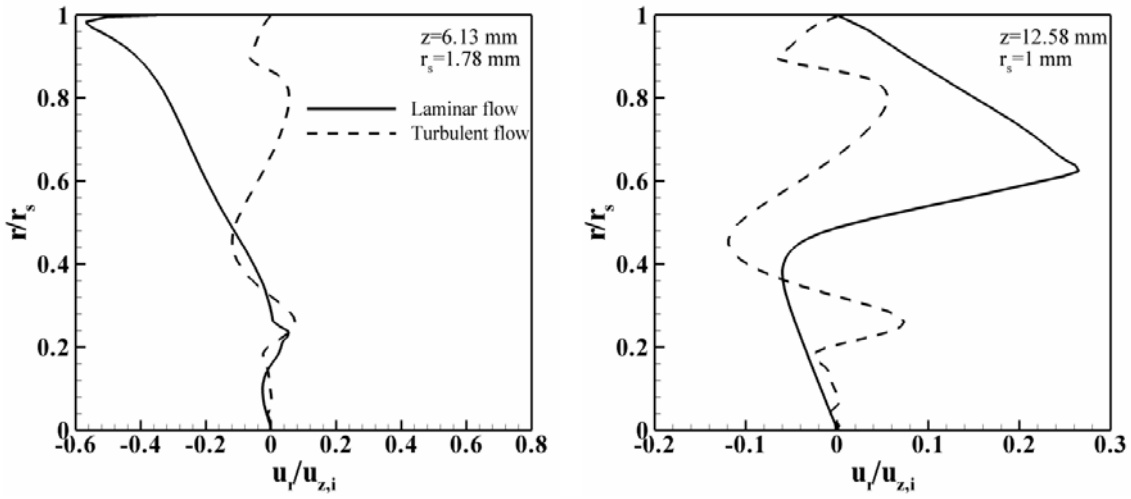

(10a) (10b)

Fig. 11 Radial velocity across the cone region at different axial locations of the nozzle

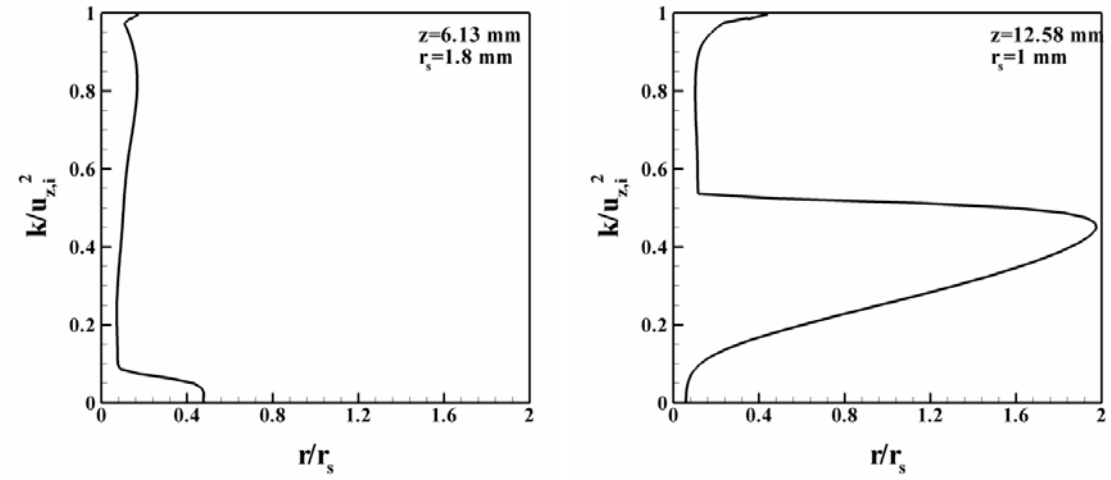

(11a) (11b)

Fig. 12 Turbulent kinetic energy in the cone region at different axial locations of the nozzle

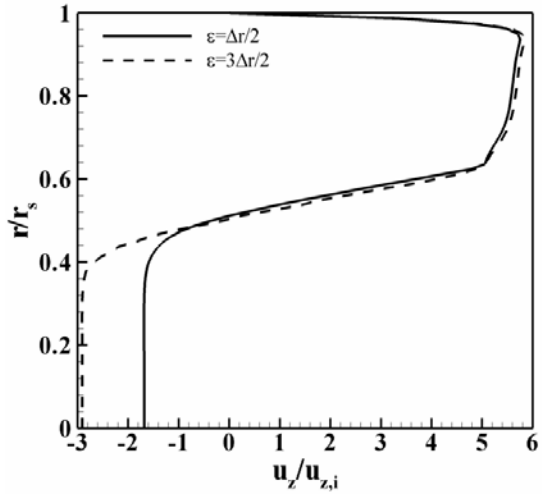

Fig. 13 Axial velocity of laminar flow for different interface thicknesses for $z = 12.56mm$ **and** $r_s = 1mm$